Journal of Power Sources 185 (2008) 1030–1039

Contents lists available at ScienceDirect

Journal of Power Sources

journal homepage: www.elsevier.com/locate/jpowsour

The behavior of nickel and silver in a simulated solid oxide fuel cell environment

R.W. Jackson*, F.S. Pettit, G.H. Meier

Department of Mechanical Engineering and Materials Science, University of Pittsburgh, Pittsburgh, PA 15261, USA

ARTICLE INFO

Article history:
Received 23 July 2008
Received in revised form 21 August 2008
Accepted 22 August 2008
Available online 28 August 2008

Keywords:
SOFC
Interconnect
Nickel
Silver
Cavitation
Water vapor

ABSTRACT

Nickel, silver, and a nickel–silver composite have been tested in a simulated solid oxide fuel cell interconnect environment. The susceptibility of the interconnect to mechanical degradation as a result of environmental attack has been analyzed. The experimental results of this study demonstrate that silver is unstable in the interconnect environment, while nickel remains stable. A finite difference model has been developed to analyze how the simultaneous diffusion of hydrogen and oxygen into the interconnect can result in the nucleation of water vapor bubbles. In addition, a model developed by Raj and Ashby to describe the growth of cavities under creep conditions has been employed to predict the rate at which cavity growth will occur. Finally, a Ni–Ag composite was fabricated and studied as an interconnect in an attempt to avoid the mechanical degradation that occurs in silver, while maintaining a path for electrical conduction that is not degraded by oxidation.

1. Introduction/background

The development of a suitable interconnect is one technological hurdle inhibiting the development of planar solid oxide fuel cells (SOFCs). The role of the interconnect is to provide an electrical connection between adjacent cells while separating the anode and cathode gases. During operation, the interconnect is simultaneously exposed to an anode gas; which has a low oxygen partial pressure, and is typically a hydrogen–water vapor mixture that may contain hydrocarbons, and a cathode gas; typically air, or pure oxygen at temperatures between 700 and 900 °C. The interconnect must be electrically conducting, mechanically stable, and must maintain compliance while thermally cycled. In addition, the interconnect must be easily fabricated and inexpensive, in order to make the cell commercially viable [1–5].

Currently, stainless steels are the alloys of choice as candidate interconnect materials because they can provide the aforementioned properties. However, the chromia scale which provides corrosion protection to these alloys releases volatile oxides which have been found to interact with the cathode, drastically decreasing cell performance [6]. While much research is being performed in order to limit the release of volatile chromium oxides through overlay coatings [7,8] and multilayer thermally grown oxides [9,10], there is motivation to examine alternate interconnect materials which do not contain chromium [11,12].

Recently, it has been found that the behavior of certain materials, exposed to the dual atmospheric environment of the SOFC, differs from their behavior when exposed to either the cathode or anode gases separately [13,14]. One example of this phenomenon occurs in ferritic stainless steels. The oxidation resistance of 430, Fe–17 Cr, is much worse when exposed to the dual atmosphere of the fuel cell, then when exposed to either the fuel or oxidant gases independently [13]. In the dual atmospheric environment, rapidly growing iron rich nodules form on the surface of the alloy exposed to the oxidant gas, and these nodules lead to premature failure of the interconnect. The mechanism which changes the oxidation behavior is not fully understood, but it is believed to result from the interaction of hydrogen, which has permeated from the fuel gas through the interconnect, with the oxide scale.

A variant of the interconnect, which has been designed to utilize the electrical properties of silver, has been proposed by Meulenberg et al. [15]. These authors fabricated a FeCrAl alloy, with silver wires passing through, which provide electrical connection between the anode and the cathode. Due to the high resistivity of the oxides that grow on high temperature alloys, an optimized noble metal–alloy composite could be a promising alternative to the conventional interconnect alloys.

However, when silver is exposed to the dual atmospheric environment, it undergoes rapid mechanical degradation [14]. The mechanical breakdown is driven by the simultaneous dissolution of oxygen from the cathode gas and hydrogen from the anode gas into

* Corresponding author at: 848 Benedum Hall, 3700 O'Hara St., Pittsburgh, PA 15261, USA. Tel.: +1 412 523 3373; fax: +1 412 624 8069.
E-mail address: rwj1@pitt.edu (R.W. Jackson).

0378-7753/$ – see front matter © 2008 Elsevier B.V. All rights reserved.
doi:10.1016/j.jpowsour.2008.08.056

the interconnect. Once oxygen and hydrogen are dissolved at sufficient concentrations, the two species react to form water vapor. The pressure of the water vapor grows to be quite large, which causes cavities to nucleate and grow [14].

Along with the interconnect, the seal components of the SOFC are also exposed to the dual atmospheric environment. One promising sealing method, the air-brazed seal, utilizes silver–copper oxide composites [15–17]. Like the silver interconnect, water vapor bubbles have been found to nucleate in the Ag–CuO air-brazed seals, but to a lesser extent.

In this paper, the behavior of nickel, silver, and nickel–silver composites, in simulated fuel cell environments is discussed with regard to their performance in an interconnect environment. The goals of the investigation are twofold: evaluating the stability of these systems in an interconnect environment, and better understanding the mechanism by which dual atmospheres degrade the interconnect.

2. Theory

An essential function of the interconnect is to maintain mechanical stability while separating the anode and cathode gases. The internal formation of water vapor bubbles is one mechanism that has been found to drastically degrade the mechanical integrity and hermeticity in materials which are exposed to the dual atmospheric environment [14,17]. It is of interest to determine under what conditions mechanical degradation will occur, and further, it is of interest to understand the mechanisms that produce this degradation.

The formation of water vapor in materials exposed to the dual atmosphere, in which cavities grow during high temperature exposure, is similar to degradation that occurs in a number of other systems in which an alloy is exposed to an atmosphere from which a gaseous species can dissolve into the alloy and react with a constituent in the alloy. Shewmon et al. [18] has termed the phenomenon chemically driven cavity growth (CDCG). A notable example of CDCG occurs when carbon steels are used as hydrogen pressure vessels. During high temperature exposure, hydrogen can dissolve into the steel, and react with the carbon in the steel to create methane. After sufficient time at temperature, methane bubbles nucleate at high pressures, which causes cavity growth, leading to a dramatic loss of ductility, and eventually failure of the vessel [19–21].

Below, the void nucleation models developed by Raj and Ashby [22,23], which were used by Shewmon [19] to model CDCG are expanded to analyze the formation of water vapor bubbles in metallic sheets which are permeated by hydrogen and oxygen from opposite sides.

2.1. CDCG in an interconnect

In order to determine if a material is susceptible to CDCG, the first step is to determine the driving force for cavity growth which is the gas pressure inside the interconnect. The water vapor pressure can be calculated, with knowledge of the concentration profiles of oxygen, and hydrogen across the interconnect, along with the equilibrium constant which governs the equilibrium of oxygen, hydrogen, and water vapor. If nucleation of water vapor bubbles occurs, the time to failure can be determined by calculating the rate at which the bubbles grow.

2.1.1. Water bubble nucleation

The solubility of diatomic gases in metals can be calculated using Sieverts's law, Eq. (1), where C_X is concentration of gas dissolved in the metal, p_{X_2} is the partial pressure of the gas in equilibrium with the metal, and S_X is a proportionality constant.

$$C_X = S_X \sqrt{p_{X_2}} \tag{1}$$

The value p_{X_2} in equilibrium with the metal can be assumed to be the partial pressure in the gas phase when no reaction product is formed on the surface of the metal, as is the case when calculating the solubility of oxygen and hydrogen in silver, and hydrogen in nickel. However, when a reaction product does form on the surface of the metal, as is the case when NiO grows on nickel exposed to the cathode gas, the oxygen pressure at the nickel surface is fixed by the Ni/NiO equilibrium.

The reaction between dissolved hydrogen and oxygen will proceed, when the free energy of the system is reduced as a result of the creation of water vapor. The change in free energy that occurs as a result of nucleation is primarily a function of three factors: the work that is done on the metal by an expanding bubble, $\Delta P\,dV$, where ΔP is the difference in pressure between the bubble and the atmosphere and V is the volume of the bubble, the increase of surface energy that results from the creation of new surface, $\gamma\,dA$, where γ is the surface free energy and A is surface area of the bubble, and the elastic strain energy that results from the expansion of the bubble, $U\,dV$, where U is the elastic strain energy density. However, U is proportional to $\Delta P^2/2E$ and when $\Delta P \ll E$, the elastic strain energy can be neglected. The change in free energy, ΔG, associated with the growth of a water vapor bubble can be expressed as Eq. (2) with the assumption that the bubbles are spherical [19,22–24].

$$\Delta G = -\frac{4}{3}\pi r^3 \Delta P + 4\pi r^2 \gamma \tag{2}$$

The critical radius r^*, the radius at which any growth will decrease the total free energy can be found by evaluating $d\Delta G/dr = 0$.

$$r^* = \frac{2\gamma}{\Delta P} \tag{3}$$

The water vapor pressure can be calculated by determining the thermodynamic relationship between dissolved hydrogen and oxygen and water vapor. The formation of water vapor, from hydrogen and oxygen gas at one atmosphere, can be expressed by the chemical reaction in Eq. (4), which is governed by the equilibrium constant K, and f_{H_2O} is the water vapor fugacity. Technically, the terms in the denominator of Eq. (4) should be fugacities, rather than pressures, but because the hydrogen and oxygen pressures are low, it is a good assumption that gases behave ideally, and that the gas partial pressure is equal to the fugacity.

$$H_{2(g)} + \frac{1}{2}O_{2(g)} = H_2O_{(g)} \qquad K = \frac{f_{H_2O}}{p_{H_2} p_{O_2}^{1/2}} \tag{4}$$

Substituting Eq. (1) into Eq. (4), the equilibrium between water vapor, and dissolved oxygen and hydrogen can be expressed, Eq. (5),

$$K = \frac{f_{H_2O}}{(C_H/S_H)^2 (C_O/S_O)} \tag{5}$$

The fugacity can be related to the pressure by the fugacity coefficient, Γ.

$$P = \Gamma f \tag{6}$$

The pressure–fugacity relationship for water vapor at high temperatures and pressures has been determined by Pistorious and Sharp [25]. This data has been interpolated to determine the pressure–fugacity relationship at the desired pressures. Using this data, the water vapor pressure can be determined as a function of

the hydrogen and oxygen concentrations.

$$K\left(\frac{C_H}{S_H}\right)^2\left(\frac{C_O}{S_O}\right)\Gamma(P) = P_{H_2O} \tag{7}$$

If a particular critical radius is designated, then a corresponding critical pressure P^*, can be determined. Using this threshold pressure, Eq. (7) can be rearranged to determine the critical solubility product.

$$(C_O^*)(C_H^*)^2 = \frac{P^*_{H_2O}S_OS_H^2}{\Gamma(P)K} \tag{8}$$

2.1.2. Concentration profiles

A finite difference model has been employed to determine the time and location at which the critical hydrogen and oxygen solubility product will occur. The concentration profiles, as a function of time, through a sheet of finite thickness, can be determined by solving Fick's second law.

$$\frac{\partial C}{\partial t} = D\frac{\partial^2 C}{\partial x^2} \tag{9}$$

If the thickness of the slab is L, the diffusion coefficient is D, then the location can be x, and the time t, can be normalized, with

$$X = \frac{x}{L}$$
$$T = \frac{Dt}{L^2}$$

Fick's law can then be rewritten

$$\frac{\partial C}{\partial T} = \frac{\partial^2 C}{\partial X^2} \tag{10}$$

The distance X, can be divided into segments δX, and the time T can be divided into intervals δT. Using the Schmidt Method [26], a Taylor expansion is performed on the left side of Eq. (10) in which the first two terms are considered, and the first three terms of the Taylor expansion are considered on the right side, producing Eq. (11).

$$C(x_i, t_{j+1}) = C(x_i, t_j) + \frac{\delta T}{(\delta X)^2}(C(x_{i-1}, t_j) - 2C(x_i, t_j) + C(x_{i+1}, t)) \tag{11}$$

In Eq. (11), the concentration of a species at location x, and time t is expressed as $C(x_i,t_j)$. The concentration at time t, and a location $x+\delta X$ is denoted $C(x_{i+1},t_j)$, while the concentration at a location x, at a time $t+\delta T$ is denoted $C(x_i,t_{j+1})$.The concentration profiles are now subject to the boundary conditions

$$\begin{array}{lll} t = t & C_O = C_O^{(S)} & \text{for } x = 0 \\ & C_H = C_H^{(S)} & \text{for } x = L \\ t = t & C_O = C_O' & \text{for } x = X \\ & C_H = C_H' & \text{for } x = X \end{array}$$

And the initial condition that

$$\begin{array}{lll} t = 0 & C_O = 0 & \text{for } x = x \\ & C_H = 0 & \text{for } x = x \end{array}$$

In the model, the simultaneous diffusion of hydrogen and oxygen is considered. It is assumed that cross-diffusion coefficients are negligible and that the creation of oxygen–hydrogen compounds other than water is not significant. Further, it is assumed that once the critical solubility product is reached, the water fugacity, and the corresponding water vapor pressure is great enough to promote nucleation of water vapor bubbles at the designated critical size. Once this critical solubility product is reached, at a given location and time, any additional oxygen and hydrogen that diffuses in, forms water. This is expressed in Eq. (12) where δ_{P^*} is a Kronecker delta function, which is equal to zero if the solubility product is less then the critical value, and 1 if it is greater.

$$C(x_i, t_{j+1}) = C(x_i, t_j) + \frac{\delta T}{(\delta X)^2}(C(x_{i-1}, t_j) - 2C(x_i, t_j) + C(x_{i+1}, t)) - \delta_{P^*}\frac{\delta T}{(\delta X)^2}(C(x_{i-1}, t_j) - 2C(x_i, t_j) + C(x_{i+1}, t)) \tag{12}$$

Therefore, the concentrations of hydrogen and oxygen dissolved in the metal will increase with time until the critical solubility product is reached, and then remain constant.

2.1.3. Cavity growth

Once the cavities have nucleated, certain processes must occur in order for growth to proceed. These processes are: [19]

(I) Movement of H to the cavity.
(II) Movement of O to the cavity.
(III) $\underline{H} + \underline{O} \rightarrow H_2O$.
(IV) Movement of metal from the cavity.

The intrinsic diffusivities of hydrogen and oxygen in metals are typically much greater than the self diffusivity of metal atoms, Table 2. In addition, the self grain boundary diffusivity is generally substantially greater than the lattice diffusivity, at SOFC operating temperatures. Therefore, the rate of cavity growth will be controlled by the movement of metal atoms away from the cavity along grain boundaries. This is not necessarily the case for silver, due to it's high self lattice diffusivity. However, using the assumption that the self grain boundary diffusion controls the cavity growth rate, the subsequent cavity growth rate calculations are greatly simplified because there is a fixed area from which the metal atoms will diffuse away from the cavity.

Following Raj and Ashby [22] and Raj et al. [23], the rate at which spherical cavities which are uniformly distributed at distance $2a$ apart, grow, when the cavities have an internal pressure P is given in Eq. (13). The derivation is presented in the Appendix.

$$\frac{dV}{dt} = \frac{2\pi D_B\delta\Omega}{kT}\left(\Delta P - \frac{2\gamma}{r}\right)\frac{1-\xi^2}{\xi^2(1-(\xi^2/4)) - (3/4) + \ln(1/\xi)} \tag{13}$$

dV/dt, the change in cavity volume with time; D_B, grain boundary self diffusivity; δ, grain boundary width; Ω, atomic volume; P, water vapor pressure in the cavity; P_{atm}, the atmospheric pressure $\Delta P - P = P_{atm}$; $2a$, inter-cavity spacing $\xi = r/a$; T, temperature; K, Boltzmann's constant.

3. Experimental procedure

The environment of the interconnect in a SOFC was simulated using two specifically designed experimental configurations, with one apparatus being designed to test sheet specimens, and the other being designed to test tube specimens. The dual atmospheric tube apparatus is shown in Fig. 1(a). In this test, two metallic tubes were fixed in a silica reaction chamber, inside a horizontal resistance furnace. One of the tubes was exposed to a dual atmosphere by flowing dry air, the simulated cathode gas (SCG), through the reaction chamber, while a simulated anode gas (SAG) was passed through the center of the tube. The second tube, used as a control, had dry air passed through its interior.

A schematic of the second dual atmospheric test configuration is shown in Fig. 1(b). In this test, one face of a sheet specimen was exposed to the SCG, while the other face was exposed to the SAG.

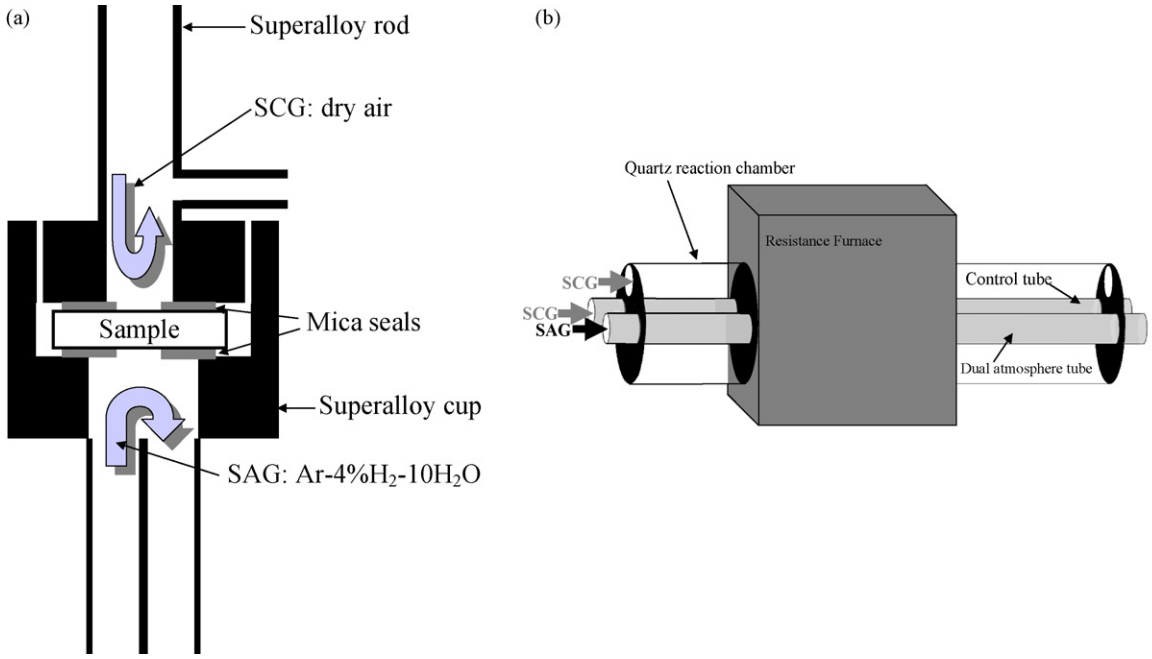

Fig. 1. (a) Tubular and (b) sheet dual atmospheric apparati.

Table 1
The composition of anode gas mixtures at 800 °C

Gas mixture	Partial pressure (atm)		
	H_2	H_2O	O_2
Simulated anode gas	0.04	0.1	2.7×10^{-18}
Typical anode gas	0.97	0.03	4.1×10^{-22}

The apparatus was constructed of nickel-base superalloys, with mica seals used to prevent the mixing of the SCG and SAG.

The SAG was a gas mixture composed of Ar–10% H_2O–4% H_2. The properties of the SOFC anode gas which our test gas was designed to simulate were twofold: the gas mixture should have a sufficiently low oxygen partial pressure, such that the metals used in this test do not oxidize, and the gas mixture should have a sufficiently high hydrogen partial pressure to produce a flux of hydrogen into the metal. The composition of the SAG is compared with the composition of a typical anode gas in Table 1. Carbon monoxide and higher hydrogen partial pressures where avoided for safety reasons.

The materials tested in these apparati were, high purity nickel sheet (99.999% pure Goodfellow Ltd.), and Ni200 a lower purity grade of nickel, in the form of tubes, silver sheets (99.99% Goodfellow), and nickel–silver composites. The nickel–silver composites were fabricated by drilling a hole in high purity nickel sheet, 400 μm in diameter and 500 μm in depth. Silver powder was placed in the hole, and then heated to 975 °C, approximately 15 °C above the melting point of silver, in Ar–4% H_2. Silver extended approximately 100 μm above the nickel surface. The initial Ni–Ag specimen was fabricated by melting the silver in one step and it is believed during this process, gas was trapped, leaving pores in the Ag. To avoid the entrapment of gas, a second specimen was fabricated by adding small amounts of silver powder and then melting. The process was repeated three times to fill the hole.

4. Results and discussion

4.1. Silver

Dual atmospheric exposures were performed at 800 °C for 1, 4, 16, and 24 h. Porosity was observed in the cross-section after the 1 h exposure and the extent of the porosity increased with the longer exposure time, as shown in Fig. 2. The porosity initiated approximately 0.7 mm from the silver surface, which was exposed to the SCG.

4.1.1. Void nucleation in silver

The solubility of oxygen in silver has been determined by Ramanarayanan and Rapp [27] and the solubility of hydrogen has been determined by Steacie and Johnson [28]. This data, along with the oxygen and hydrogen diffusivity in silver are presented in Table 2. Using the finite difference model developed in Section 2.1.2, the hydrogen and oxygen concentrations across the 1 mm sheet of silver can be calculated, and from these values, the equilibrium water vapor fugacity and pressure can be determined.

The equilibrium water vapor pressure will increase as the oxygen and hydrogen concentrations increase until a critical pressure is reached at which water vapor bubbles will nucleate. As shown by Eq. (3), the higher the water vapor pressure, the smaller the critical radius becomes. However, because a minimum cavity radius could not be experimentally observed, an assumption for the critical radius must be made. It is assumed that the critical radius is 0.35 nm, which is slightly larger than radius of two water molecules, and corresponds to a critical pressure of 6.6 GPa.

It should be noted that the model is sensitive to the choice of critical radius. If values of the critical radius are chose to be smaller than 0.3 nm, the corresponding critical water vapor pressure will not be reached, even when steady-state oxygen and hydrogen concentration profiles have developed. Conversely, if the critical radius is assumed to be larger than 0.5 nm, water nucleation will occur after only 10 s, and the location of nucleation will be 0.1 mm from the silver–SCG interface. The model fits the experimental results best if a critical radius of 0.35 nm is chosen and while this choice is arbitrary, it is a reasonable nucleus size for homogeneous nucleation under a large driving force [29].

Fig. 3 presents the calculated water vapor pressure, normalized by the critical pressure, through the thickness of the interconnect as a function of time. The critical pressure for water vapor nucleation is reached after 107 s, 0.55 mm from the silver surface exposed to the cathode gas.

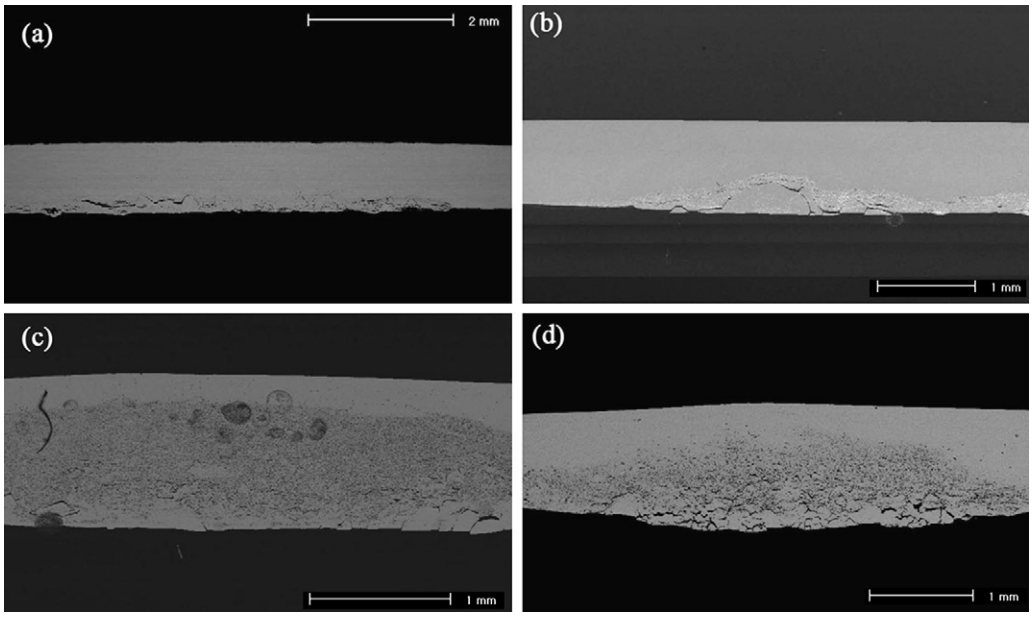

Fig. 2. Silver exposed for (a) 1 h (lower magnification); (b) 4 h; (c) 16 h; and (d) 24 h to dry air on the upper surface and Ar–4% H_2–10% H_2O on the lower surface at 800 °C.

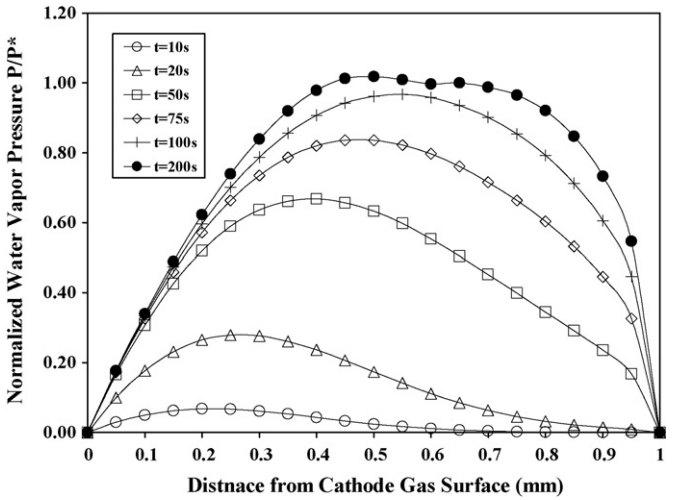

Fig. 3. Modeled normalized water vapor pressures across a silver interconnect, exposed at 800 °C, with a SCG of air and an SAG of Ar–4% H_2–10% H_2O at 800 °C.

As seen in Fig. 2, after 1 h cavitation is observed to have initiated roughly 0.75 mm from the cathode gas side of the interconnect. Based on the respective diffusivities of oxygen and hydrogen in silver, Table 2, one might expect that water nucleation should occur near the SCG/silver interface. However, because the solubility of oxygen in silver is greater than that of hydrogen, and because a 2:1 ratio of hydrogen to oxygen is needed to form H_2O, nucleation occurs closer to the hydrogen source, the SAG/silver interface, than the SCG/silver interface.

By fixing the critical radius at 0.35 nm, the critical water vapor pressure is a significant fraction of the Young's Modulus [30]. As a result, the elastic strain energy associated with nucleation may not be discounted on the $P \ll E$ criterion given in Section 2.1.1 However, using the nucleation model of Hirth and Nix [24] in which the elastic energy is taken into account, the change in critical radius when keeping the pressure at a given value, is only tenths of a nanometer. Given the uncertainty in the interpolation of pressure–fugacity data, we deem that the increase in complexity of the nucleation model, which results from the inclusion of elastic strain energy is not justified.

Using the above assumptions, the model predicts the location of the water vapor front with reasonable accuracy. However, the model predicts the expansion of the water vapor zone, to be more rapid, then was experimentally observed.

4.1.2. Void growth in silver

The rate of void growth can be calculated using Eq. (13), starting with different internucleation site distances and the results are presented in Fig. 4. This analysis predicts that the cavity radius will grow to reach the internulceation site distance, resulting in coalescence, in less than 1 h. Fig. 5 shows the presence of cavities throughout the silver and it appears the cavity coalescence has occurred along grain boundaries after 1 h. The calculated cavity growth rate predicts more rapid cavity growth than was experimentally determined. However, it is clear that a pure silver interconnect could not survive in a fuel cell environment for any substantial fraction of the desired 40,000 h lifetime.

Table 2
The diffusivity and maximum concentration of hydrogen, and oxygen, in nickel and silver, respectively, under dual atmospheric conditions at 800 °C

Species	Nickel 800 °C		Species	Silver 800 °C	
	Diffusivity, D ($cm^2\ s^{-1}$)	Concentration, C ($mol\ cm^{-3}$)		Diffusivity, D ($cm^2\ s^{-1}$)	Concentration, C ($mol\ cm^{-3}$)
Self GB	1.76×10^{-7}	6.59	Self GB	2.18×10^{-6}	10.27
Hydrogen	6.88×10^{-5}	1.37×10^{-5}	Hydrogen	2.93×10^{-4}	6.14×10^{-7}
Oxygen	7.07×10^{-10}	2.67×10^{-5}	Oxygen	1.06×10^{-5}	1.14×10^{-5}

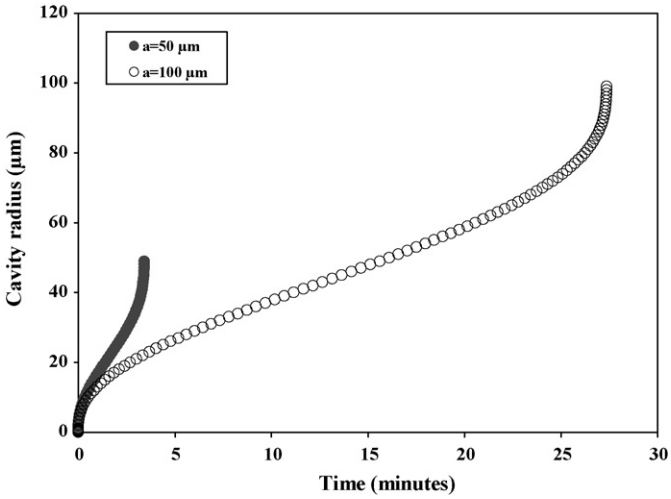

Fig. 4. The predicted change in cavity radius as function of time for a silver interconnect, exposed at 800 °C, with a SCG of air and an SAG of Ar–4% H_2–10% H_2O.

4.2. Nickel

The performance of nickel under the simulated dual atmosphere was studied using both experimental configurations shown in Fig. 1. Nickel 200 tubes were exposed at 800 °C for 400, and 600 h. The cross-sectional images of the specimen exposed for 600 h are shown in Fig. 6. The nickel tube in Fig. 6(a) was exposed to the SCG on the inside and the outside of the tube and NiO grew on both sides. The nickel tube in Fig. 6(b) was exposed to the SAG on the inside and the SCG on outside of the tube. NiO grew on the outside of the tube, but no oxidation occurred on the inner wall. The growth of NiO on the tube exposed to the dual atmosphere was nearly identical to the NiO formed on the tube exposed to air on both sides with slightly less porosity occurring at the Ni/NiO interface for the dual atmosphere specimen. Also, no porosity is observed in the wall of the nickel tube.

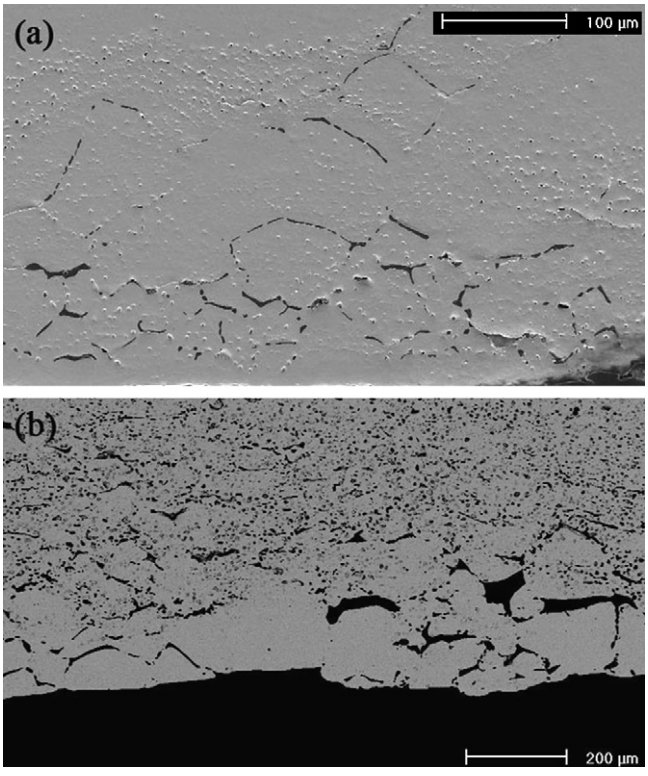

Fig. 5. Cross-sectional micrographs of silver following dual atmospheric exposure for (top) 1 h and (bottom) 24 h.

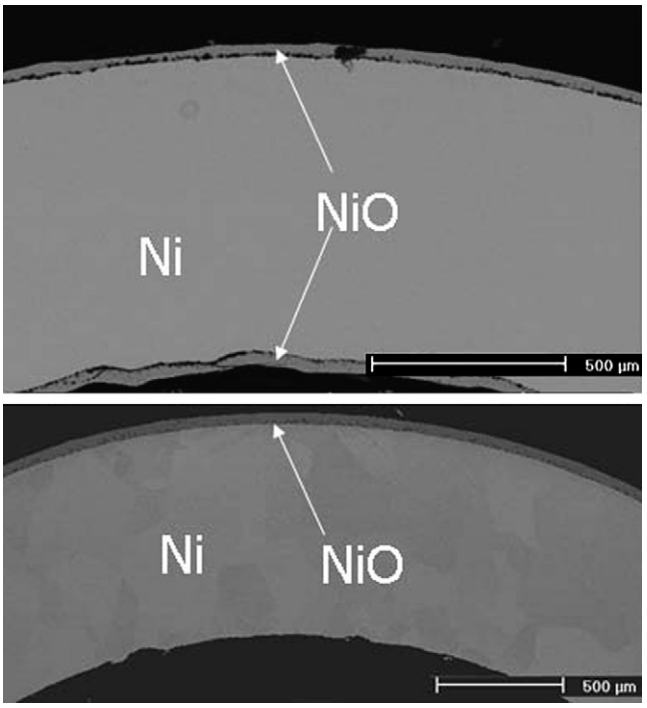

Fig. 6. Nickel exposed at 800 °C for 600 h (Top) to dry air on the inside and the outside of the tube and (Bottom) exposed to dry air on the outside of the tube and Ar–4% H_2–10% H_2O on the inside.

4.2.1. Void nucleation

While no cavity formation was observed in nickel exposed to the simulated dual atmosphere, it is of interest to calculate what the driving force for water formation was under the current experimental conditions. It is also of interest to calculate how the driving force for water vapor formation will change in the higher hydrogen environment, typical of operational SOFCs.

The solubility of oxygen in nickel has been determined by Park and Altsetter [31] and the solubility of hydrogen has been determined by Jones and Pehlke [32]. This data along with the oxygen and hydrogen diffusivity in nickel are presented in Table 2. The concentration profiles are presented in Fig. 7. In the analysis of silver in the dual atmosphere, it was assumed that the concentration of the dissolved species on the opposite surface goes to zero. This assumption is good because the flowing gas across the surface will remove the dissolved species much faster than it can be replenished by solid-state diffusion. This assumption should also apply to the removal of oxygen from nickel into the anode gas. The approximation of the hydrogen concentration at the Ni/NiO is less straightforward due to the unknown permeability of hydrogen through NiO. However, the limiting cases of infinitely fast diffusion through the NiO scale, leading to a zero concentration at the interface and, infinitely slow diffusion, leading to a constant hydrogen concentration can be analyzed. The oxygen and hydrogen concentration profiles across nickel, presented in Fig. 7 were used to determine the water vapor fugacity across the thickness of the nickel, presented in Fig. 8. When the hydrogen concentration is assumed to go to zero at the Ni/NiO interface, the maximum fugacity occurs near the center of the nickel sheet and is a little less than 0.1 MPa. Under these conditions the water vapor pressure never exceeds the atmospheric pressure, and

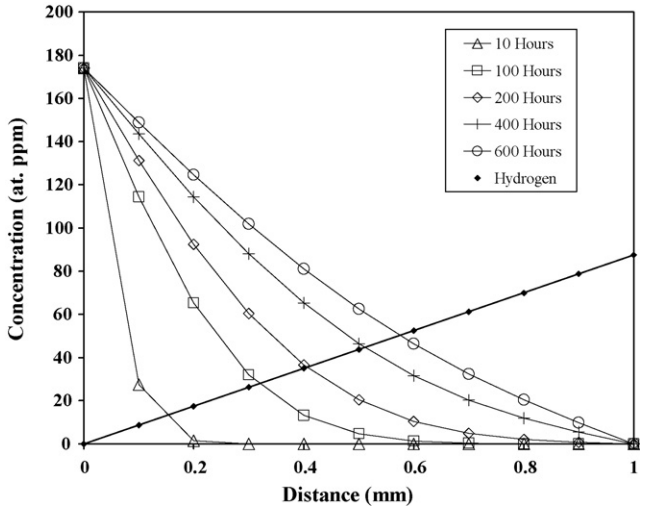

Fig. 7. Calculated oxygen and hydrogen concentration profiles across a 1 mm thick nickel sheet exposed at 800 °C at a SCG of air and an SAG of Ar–4% H_2–10% H_2O.

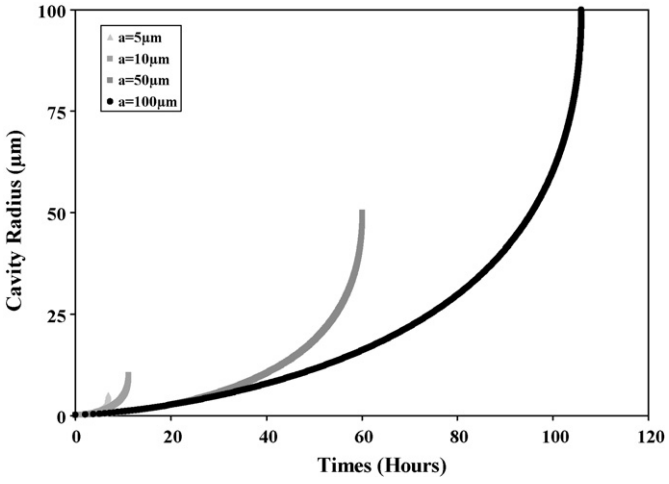

Fig. 9. The predicted change in cavity radius as a function of time in nickel at 800 °C exposed to 1 atm H_2. It is assumed that the hydrogen pressure is constant throughout the nickel specimen.

as a result, there was no driving force for cavity nucleation. In the other limiting case, in which NiO blocks hydrogen diffusion, the water vapor fugacity was a maximum at the Ni/NiO interface and equal to 0.7 MPa. Under these conditions, the fugacity can be equated to the pressure and the critical radius for water vapor nucleation was 5 μm. This critical radius is quite large, and this explains why no water vapor bubbles were observed in nickel. If nickel was exposed to 1 atm of hydrogen as opposed to the 0.04 atm used in this study, the maximum water pressure would be 17 MPa, if hydrogen is blocked by NiO, and the corresponding critical radius would be 0.22 μm. This value is still rather large, however, during oxidation, voids have been observed to form at nickel grain boundaries that result from an injection of vacancies which occurs during oxidation [33]. If this occurred, it is possible that nucleation could result.

4.2.2. Void growth in nickel

If void nucleation can occur in nickel, it is of interest to determine the rate at which such a cavity would grow. The rate of cavity growth in nickel is plotted for different internucleation site distances in Fig. 9 which shows that the cavities will grow to a point of coalescence, at $r = a$, in less than 150 h, even for large internucleation site distances. Fig. 8 shows that it takes over 600 h in order for the steady-state diffusion profile to be established. This is the condition at which a maximum pressure is developed. Therefore, the total time until void coalescence could be on the order of 750 h.

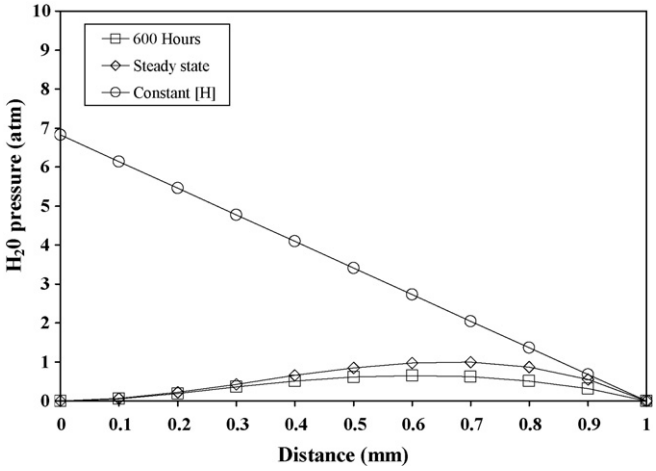

Fig. 8. Calculated water vapor pressures across a 1 mm nickel sheet.

4.3. Silver–nickel composites

A nickel–silver composite was developed to create an interconnect capable of maintaining a metallically conducting pathway between the anode of one cell and the cathode of an adjacent cell, that does not allow the mixing of the anode and cathode gases. The nickel–silver interconnect consists of a sheet of nickel, the plane of the sheet being parallel with the other components of the planar SOFC, with a cylindrical section of silver extending from above the nickel sheet on the cathode side of the interconnect, halfway through the sheet. A schematic of the silver–nickel composite interconnect in a planar SOFC stack is shown in Fig. 10.

The nickel–silver composite was exposed to dual atmospheric conditions for 100 h at 800 °C. Cross-sectional micrographs are shown in Fig. 11. In Fig. 11(a) a large pore is located in the middle of the silver. This pore is believed to be the result of gas which was trapped during fabrication. Fig. 11(b) shows the cross-section of the Ni–Ag component, in which the silver was applied incrementally, after a 100 h exposure in dual atmospheric conditions, at 800 °C.

Fig. 12 shows the cross-section at higher magnification. It can be seen that oxidation occurs at the nickel–silver interface and can be attributed to the high flux of oxygen through silver. However, conductivity measurements taken at room temperature show that good conductivity remained through the sample. This result can be

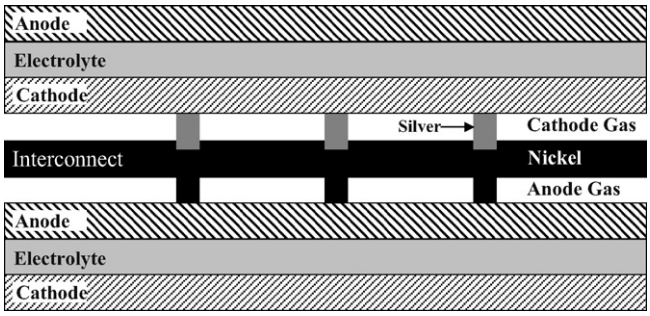

Fig. 10. A schematic of the Ni–Ag composite in a planar SOFC stack.

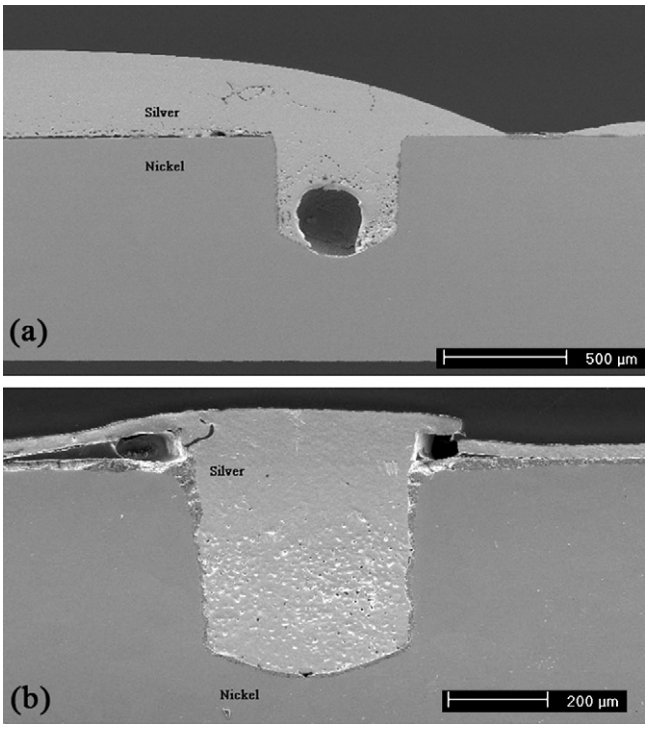

Fig. 11. High conductivity Ni–Ag composite exposed to dual atmospheric conditions, SCG on the top of the figure and SAG at the bottom, for 100 h at 800 °C. In (a) silver applied in one melting step and in (b) silver was applied in three melting steps.

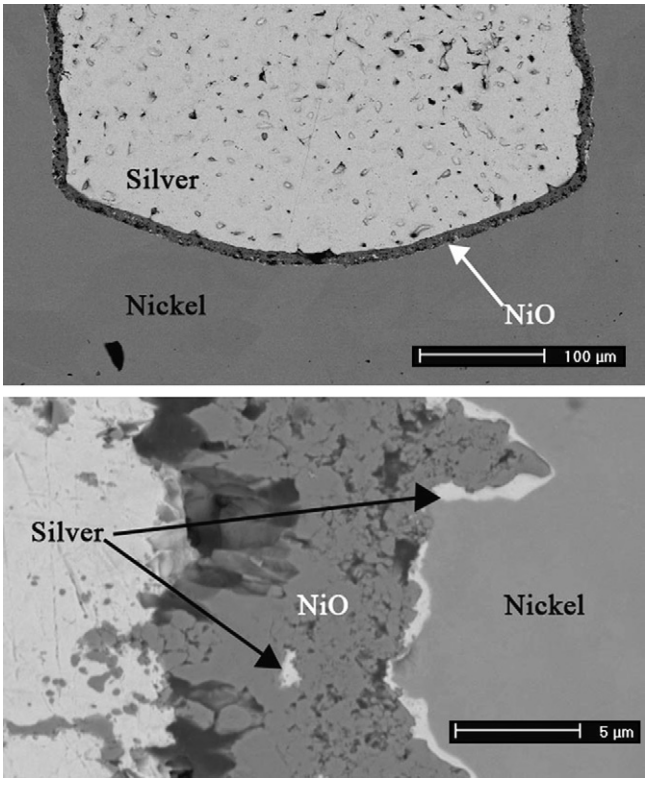

Fig. 12. Ni–Ag composite exposed to dual atmospheric conditions for 100 h at 800 °C.

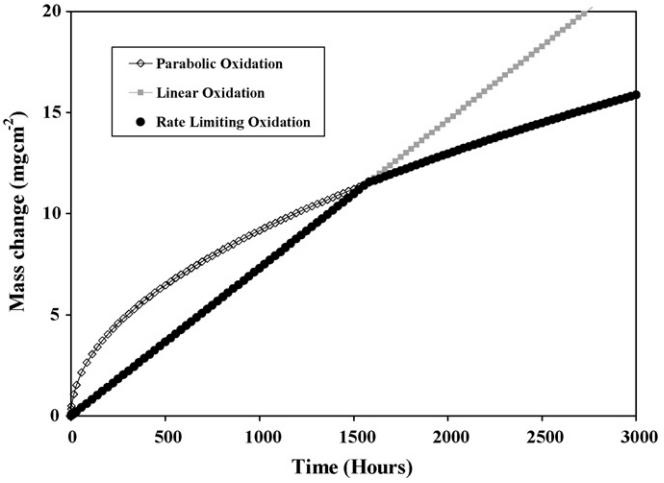

Fig. 13. Calculated nickel oxide growth at 800 °C when nickel is coated by a 600 μm thick silver layer.

attributed to an electrical short circuit path remaining at the silver nickel interface at which oxidation did not occur.

Nickel oxide was observed to grow at the nickel–silver interface, Fig. 12, in the Ni–Ag composite system. The desired function of the composite was to avoid the resistive degradation that results from oxidation without making an interconnect solely from a precious metal. However, it is clear that the resistance of this system will still be controlled by the rate of oxidation.

After the 100 h exposure, the NiO scale, grown beneath the silver layer is about 5 μm thick, while NiO grown on uncoated nickel is approximately 20 μm thick. It is of interest to analyze the rate of oxide growth in the Ni–Ag system as a function of time.

When NiO grows on a nickel, the growth rate of NiO can be controlled by one of three processes: the incorporation of metal into the oxide scale at the metal/oxide interface, the incorporation of oxygen at the external surface of the oxide, or by diffusion through the oxide. The flux of Ni through NiO is inversely proportional to oxide thickness, and after long exposure times, when the NiO scale is thick; the growth of NiO will be controlled by the diffusion in the oxide In this case, the growth kinetics follow the parabolic rate law, Eq. (14) where Δm ($g\,cm^{-2}$) is the change in mass per unit area, and k_p'' ($g^2\,cm^{-2}\,s^{-1}$) is the parabolic rate constant [33].

$$\Delta m^2 = k_p'' t \tag{14}$$

When the flux of oxygen to the NiO oxide surface is slow, such as when nickel is cover by a layer of silver, the growth of NiO will be controlled by the flux of oxygen to the NiO–Ag interface. The flux of oxygen through silver can be expressed using Fick's first law, Eq. (15), where C_O^S is the solubility of oxygen in silver at the silver–gas interface, C_O' is the oxygen concentration at the Ag–NiO interface and the D_O is the diffusivity of oxygen in silver.

$$J_O = -D_O \frac{\partial c}{\partial x} = D_O \frac{C_O^S - C_O'}{x} \tag{15}$$

The limiting case of oxygen-diffusion-in-silver controlled NiO growth would occur when C_O' approaches zero. The mass changes that occurs from the formation of NiO controlled by the diffusion of oxygen through silver is expressed in Eq. (16)

$$\Delta m = D_O \frac{C_O^S}{x} t \tag{16}$$

which is plotted along with the parabolic growth of NiO described by Eq. (14) in Fig. 13. The overall rate of NiO growth will be controlled by the slower process, as indicated by the bold line.

The mass change due to the formation of NiO after a 100 h exposure at 800 °C, as calculated by Eq. (16), is 0.73 mg cm^{-2}. If the NiO formed is assumed to be a dense scale, this mass change corresponds to a thickness of 5.1 μm. As seen in Fig. 12, the agreement between calculation and experiment is good.

In Fig. 13, the transition from linear to parabolic kinetics is abrupt, while in actuality, the transition is gradual, as derived by Pettit and Wagner [34]. However, using the above approximation, the linear to parabolic transition should occur after approximately 1500 h. Therefore, the NiO thickness, and the resistive contribution of the interconnect to the SOFC, is reduced during the initial period of exposure, but at long times the thickness of NiO growing at the Ag–Ni interface will be equal to the thickness of NiO growing on pure nickel. The period of reduced oxide growth rate is substantially less than the 40,000 h lifetime which is targeted for SOFC operation.

An alternative to the Ni–Ag composite which may have superior properties is a Ni–Au composite. The low permeability of oxygen through gold would severely inhibit the oxidation of nickel. The performance of this interconnect would only degrade by Ni–Au interdiffusion.

5. Conclusions

Nickel, silver, and nickel–silver composites have been tested in a simulated solid oxide fuel cell interconnect environment. The susceptibility of the interconnect to mechanical degradation as a result of chemically driven cavity growth has been analyzed. The results of this study demonstrate that silver is unstable in the SOFC dual atmospheric environment, in agreement with the earlier work of Singh et al. [14]. The time and location at which water vapor nucleation will occur was analyzed using a finite difference model. The model predicts the location of nucleation with reasonable accuracy. Nickel did not undergo mechanical degradation in the simulated interconnect environment used in this study, but calculations show that nickel may be susceptible to CDCG when pure hydrogen is used as an anode gas. Further, the rate at which cavities would grow in nickel and silver has been analyzed using a model developed by Raj and Ashby, and Shewmon. This model over-predicts the cavity growth rate in silver, and predicts that if cavities form in nickel, coalescence will occur in under 1000 h, well below the desired lifetime.

In addition to describing the degradation of the interconnect, the models developed in this paper may be applicable to the study of the degradation of brazed seals in planar SOFCs, which are also exposed to the dual atmospheric environment.

Finally, a Ni–Ag composite was studied as an interconnect that resists the mechanical degradation that occurs in silver, yet allows a path for electrical conduction that is not degraded by oxidation. In this experimental work, the Ni–Ag composite maintained metallic conductivity. However, it appears that after longer exposure times, there will no longer be continuous metallic pathways through the interconnect, and the electrical resistance of the interconnect will be controlled by the rate of oxidation of nickel.

Acknowledgement

This research was funded by the Departments of Energy as part of the Solid State Energy Conversion Alliance DOE Award: DEFC26 02NT41578.

Appendix A

This derivation of the rate of cavity growth of a pressurized cavity directly follows the work of Raj and Ashby [22], and Raj et al. [23]. The excess chemical potential $\Delta\mu$ (J atom^{-1}) of the atoms in the boundary of the cavity, relative to the stress free state is

$$\Delta\mu = -T(n)\Omega = -P\Omega \tag{A.1}$$

where Ω is the atomic volume (m^3), and $T(n)$ is the normal traction at the cavity grain boundary, which is equal to, P the internal gas pressure (Pa). The transport equation governing grain boundary diffusion under this potential gradient is then Eq. (A.2), where j_B (atoms cm^{-2} s^{-1}) is the flux of metal atoms along the grain boundary, D_B is the grain boundary diffusivity (m^2 s^{-1}) k is Boltzmann's Constant (J atom^{-1}), and R is the distance from the center of the cavity (m).

$$j_B = \frac{-D_B}{kT\Omega}\frac{\partial\Delta\mu}{\partial R} \tag{A.2}$$

Under steady-state conditions, the grain boundary flux will be a constant, β which is equal to the number of atoms removed when the boundary.

$$\frac{\partial j_B}{\partial R} = \beta \tag{A.3}$$

Combining Eqs. (A.2) and (A.3) produces Eq. (A.4).

$$\frac{\partial^2\Delta\mu}{\partial R^2} = \frac{\beta kT\Omega}{D_B} \tag{A.4}$$

Eq. (A.4) is subject to the boundary conditions: at the mid point between two bubbles a, the diffusion potential is at a minimum,

$$\frac{\partial\Delta\mu}{\partial r} = 0 \quad \text{at } R = a \tag{A.5}$$

and the diffusion potential at the cavity surface r is equal to the internal pressure minus the surface energy increase that results from the surface curvature.

$$\Delta\mu = \Omega\left(P - \frac{2\gamma}{r}\right) \quad \text{at } R = r \tag{A.6}$$

Double integration of Eq. (A.4) produces an expression which describes the potential as a function of distance R, $\Delta\mu(R)$.

$$\Delta\mu(R) = \frac{-\beta kT\Omega}{4D_B}(R^2 - r^2) - \frac{\beta kT\Omega a^2}{2D_B}\ln\left(\frac{r}{R}\right) + \Omega\left(P - \frac{2\gamma}{r}\right) \tag{A.7}$$

In this expression, the constant β which is equal to the number of atoms removed when the boundary has a thickness δ (m) is expressed as Eq. (A.8) where δ is the grain boundary width, and dV/dt (m^3 s^{-1}) is the rate of bubble growth [20].

$$\beta = \frac{dV/dt}{\delta\pi(a^2 - R^2)} \tag{A.8}$$

Further, mechanical equilibrium must be maintained such that the force produced by the internal pressure and the surface energy must be equal to the force that pushes atoms out through the grain boundary [23]. This is expressed as Eq. (A.9).

$$\pi a^2 P_{ext} + \left(P - \frac{2\gamma}{r}\right)\pi r^2 = \int_r^a \frac{\Delta\mu}{\Omega} 2\pi R^2\, dR \tag{A.9}$$

The solution to Eq. (A.9) then becomes Eq. (A.10) which describes the rate of bubble growth where $\xi = r/a$.

$$\frac{dV}{dt} = \frac{2\pi D_B\delta\Omega}{kT}\left(\Delta P - \frac{2\gamma}{r}\right)\frac{(1-\xi^2)}{\xi^2(1-(\xi^2/4)) - (3/4) + \ln(1/\xi)} \tag{A.10}$$

References

[1] W.C. Zhu, S.C. Deevi, Mater. Sci. Eng. A348 (2003) 227.
[2] W.J. Quadakkers, J. Piron-Abellan, V. Shemet, L. Singheiser, Mater. High Temperature 20 (2003) 115.
[3] Z.G. Yang, K.S. Weil, D.M. Paxton, J.W. Stevenson, J. Electrochem. Soc. 141 (2003) A1188.
[4] K. Huang, P.Y. Hou, J.B. Goodenough, Solid State Ionics 129 (2000) 237.
[5] S. Fontana, R. Amendola, S. Chevalier, P. Piccardo, G. Caboche, M. Viviani, R. Molins, M. Sennour, J. Power Sources 171 (2007) 652.
[6] K. Hilpert, D. Das, M. Miller, D.H. Peck, R. Weiss, J. Electrochem. Soc. 143 (1996) 3642.
[7] K. Huang, P.Y. Hou, J.B. Goodenough, Mater. Res. Bull. 36 (2001) 81.
[8] Z. Yang, G. Xia, G.D. Maupin, J.W. Stevenson, Surf. Coat. Technol. 201 (2006) 4476.
[9] S.P. Simmer, M.D. Anderson, G. Xia, Z. Yang, L.R. Pederson, J.W. Stevenson, J. Electrochem. Soc. 152 (2005) A740.
[10] S.J. Laney, Ph.D. Thesis, University of Pittsburgh, Pittsburgh, 2006.
[11] M.P. Brady, B.A. Pint, Z.G. Lu, J.H. Zhu, C.E. Milliken, E.D. Kreidler, L. Miller, T.R. Armstrong, L.R. Walker, Oxid. Met. 65 (2006) 237.
[12] R.W. Jackson, J.P. Leonard, F.S. Pettit, G.H. Meier, Solid State Ionics, doi:10.1016/j.ssi.2008.07.011.
[13] Z. Yang, M.S. Walker, P. Singh, J.W. Stevenson, T. Norby, J. Electrochem. Soc. 151 (2004) B669.
[14] P. Singh, Z. Yang, V. Viswanathan, J. Stevenson, J. Mater. Eng. Perf. 13 (2004) 287.
[15] W.A. Meulenberg, O. Teller, U. Flesch, P. Buchkremer, D. Stover, J. Mater. Sci. 36 (2001) 3189.
[16] K.S. Weil, C.A. Coyle, J.T. Darsell, G.G. Xia, J.S. Hardy, J. Power Sources 152 (2005) 97.
[17] J.Y. Kim, J.S. Hardy, K.S. Weil, Int. J. Hydrogen Energy 32 (2007) 3655.
[18] P.G. Shewmon, H. Lopez, T.A. Parthasarathy, Scripta Metall. 17 (1983) 39.
[19] P.G. Shewmon, Metall. Trans. 7A (1976) 279.
[20] S.S. Vagarali, G.R. Odette, Metall. Trans. 12A (1981) 2071.
[21] B.F. Dyson, Acta Metall. 30 (1982) 1639.
[22] R. Raj, M.F. Ashby, Acta Metall. 23 (1975) 653.
[23] R. Raj, H.M. Shih, H.H. Johnson, Scripta Metall. 11 (1977) 839.
[24] J.P. Hirth, W.D. Nix, Acta Metall. 33 (1985) 359.
[25] C.W.F.T. Pistorious, W.E. Sharp, Am. J. Sci. 258 (1960) 757.
[26] J. Crank, The Mathematics of Diffusion, Oxford University Press, London, 1956.
[27] T.A. Ramanarayanan, R.A. Rapp, Metall. Trans. 3A (1972) 3239.
[28] E.W. Steacie, F.M.G. Johnson, Proc. R. Soc. A117 (1928) 662.
[29] H.I. Aaronson, F.K. LeGoues, Metall. Trans. 23A (1992) 1915.
[30] H.J. Frost, M.F. Ashby, Deformation-Mechanism Maps, Pergamon Press, Oxford, 1982.
[31] J.H. Park, C.J. Altstetter, Metall. Trans. 18A (1987) 43.
[32] F.G. Jones, R.D. Pehlke, Metall. Trans. 2A (1971) 2655.
[33] N. Birks, G.H. Meier, F.S. Pettit, Introduction to the High Temperature Oxidation of Metals, Cambridge University Press, Cambridge, 2006.
[34] F.S. Pettit, J.B. Wagner Jr., Acta Metall. 12 (1964) 35.